Structural Role of CaF_2 Upon Welding Flux Viscosity

Deciphering the role of CaF_2 in welding flux viscosity: a structural bonding inquiry into polyhedra and clusters

BY H. YUAN, Y. ZHANG, Y. ZHAO, J. LI, Z. LI, AND C. WANG

Abstract

Flux viscosity affects weldability and alloying element transfer behaviors during submerged arc welding of grades of thick shipbuilding steel. It is widely accepted that viscosity is intrinsic to F-related bond structures. However, a validated relationship of the interplay remains at large. This investigation demonstrates the structure-viscosity correlation by employing experimental measurements coupled with molecular dynamics calculations. The results showed that the maximum viscosity at 1500°C decreased from 4.53 to 0.375 Pa·s as the CaF_2 content increased from 20 to 40 wt-%. Such a reduction could be partly attributed to the structures' dilution effect and the highly polymerized units' inhibition. Furthermore, CaF_2 additions introduced Ca^{2+} and F^- with high migration rates and promoted void formations among polyhedra, thereby significantly enhancing the overall diffusion coefficients from 0.25 to 2.47 $Å^2$/ns. It was also found that F^- tends to be incorporated into [AlO_n] polyhedra, with Ca^{2+} providing prominent structural compensation in Al_2O_3-rich environments. Moreover, CaF_n clusters were more favored than MgF_n clusters across all involved compositions. The findings corroborated the relationship between structural features and fluoride content. Such insights could enrich our understanding of CaF_2-induced viscosity behaviors and offer viable strategies for designing welding fluxes from an intrinsic structural perspective.

Keywords

- Welding Flux
- Viscosity
- CaF_2
- Structure
- Molecular Dynamics

Introduction

High heat input submerged arc welding is one of the most popular welding techniques for joining oil and gas pipelines and shipbuilding steels (Refs. 1–3). However, successfully demonstrating such a technique relies heavily on selecting suitable welding fluxes (Refs. 4, 5). Commercial fluxes derived from CaF_2–SiO_2–Al_2O_3–MgO systems possess physicochemical properties to protect the weld pool from the atmosphere, refine the weld metal (WM) via element transfer, and minimize heat loss through thermal insulation (Refs. 1, 6, 7). Viscosity is one of the most important properties of welding fluxes as it can dictate weldability and the transfer behaviors of alloying elements (Refs. 8, 9). Such properties are directly linked to the atomic structures of involved molten fluxes and are essentially governed by internal bond characteristics (Refs. 10–12).

CaF_2 is one of the most employed components in fluxes, serving as an effective agent to modify viscosity and limit oxygen transfer into the WM (Ref. 13). However, incorporating CaF_2 into the oxide system can cause wild fluctuations in viscosity (Refs. 14, 15), and the specific structural characteristics through which CaF_2 controls viscosity remain unclear. Previous studies suggested that CaF_2 could form CaF_n clusters, diluting the oxide network structure and lowering overall viscosity (Ref. 8). In addition, F^- ions might replace O^{2-} ions or be embedded directly into polyhedral structures, incurring unexpected structural distortions (Ref. 16). Nuclear magnetic resonance (NMR) spectroscopy can determine bonding arrangements because of high sensitivity to bond characteristics (Refs. 13, 16). Available ^{19}F NMR experiments have shown that F^- typically bonds with metal cations, such as Ca^{2+} and Na^+, rather than

https://doi.org/10.29391/2025.104.013

Table 1 — Chemical Compositions of the Welding Fluxes (Mass-%)

No.	Component			
	SiO_2	Al_2O_3	MgO	CaF_2
F20-Mg	36	8	36	20.0
F20-Al	36	35.4	8.6	20.0
F20-Si	56.5	14.9	8.6	20.0
F30-Mg	31.5	7.0	31.5	30.0
F30-Al	31.5	31.0	7.5	30.0
F30-Si	49.5	13.0	7.5	30.0
F40-Mg	27	6	27	40.0
F40-Al	27	26.6	6.4	40.0
F40-Si	42.4	11.1	6.4	40.0

Si^{4+} (Ref. 17). However, multiple NMR results have identified Si-F bonds in F-rich regions (Refs. 16, 18). Recently, molecular dynamics (MD) simulations, known for high efficiency and quantitative precision, have been widely applied to probe molten silicate structures (Refs. 19–21). By reproducing the local environment of F^- in bioactive glass, it has been suggested that F^- could replace O^{2-} in $[SiO_4]$ tetrahedron to form $[SiO_3F]$ tetrahedra (Ref. 22). With increasing temperature, F^- is more likely to integrate into high coordination silicate polyhedra ($[Si-(O, F)_n]$, $n > 4$) (Ref. 23). Furthermore, F^- has been shown to mainly diffuse with Ca^{2+} and occasionally bond with Si^{4+} and Al^{3+} in CaF_2-containing flux systems (Refs. 7, 24). Findings so far have demonstrated that the bonding patterns of F^- vary across different systems, warranting further systematic investigation.

Targeted structures are generally composed of rigid frameworks of polyhedra interspersed with wandering ionic clusters. Theoretically, increasing rigid polyhedra should raise viscosity, while a decrease should substantially lower the corresponding value (Ref. 25). Previous investigations have either focused on types and quantities of polyhedra or qualitatively attributed viscosity reduction to the dilution effect of clusters. However, it has been well suggested that both factors jointly control viscosity variations (Ref. 24). For example, network connectivity of polyhedra has been demonstrated to alter the diffusion capability of cluster ions (Ref. 7). The combined effect of polyhedra and cluster characteristics on viscosity has not been systematically explored.

In our previous investigation (Ref. 24), we established a quantitative relationship between the CaF_2–SiO_2–Al_2O_3–MgO flux structure and viscosity with constant CaF_2 fractions through atomic energy calculations and bonding characteristics. This study attempts to shed light on the effect of CaF_2 fractions on structural evolutions in light of polyhedra and cluster characteristics, thereby determining the exact relationship between flux viscosity and structure. To this end, viscosity was first measured, followed by molecular dynamics simulations for a quantitative structural analysis and diffusion pattern of polyhedra and clusters. What sets this study apart from earlier research is that we focused on the structural role of CaF_2 and distinguished the unique viscosity contributions from polyhedra and clusters.

Research Methodology

Sample Preparation

Reagent grade (> 99.9%) chemicals of SiO_2, CaF_2, MgO, and Al_2O_3 (Sinopharm Chemical Reagent Co. Ltd., Shenyang, China) were used in the synthetization of the fluxes. The powders were mixed and placed into a molybdenum crucible. Then, the mixed powder samples were premelted in a silicon-molybdenum resistance furnace under a high-purity argon atmosphere by holding the sample at 1500°C for 30 min. Afterward, the liquid fluxes were immediately quenched into cold water. The quenched samples were dried at 150°C for 4 h to remove any moisture and subsequently crushed for 30 min. The resulting powders were further sieved to obtain particle sizes < 74 μm. The chemical compositions of the targeted fluxes are shown in Table 1.

Notably, the CaF_2 content in fluxes was generally less than 40 wt-% (unless otherwise stated, all component percentages in this work are by mass) to ensure adequate coverage for the weld pool. In addition, fluxes with less than 10% of CaF_2 are difficult to fully melt at 1500–1600°C based on thermodynamics calculations using FactSage software (Version 8.1 with FactPS and FToxid databases). Our recent investigation showed that extremum viscosity values typically occur in

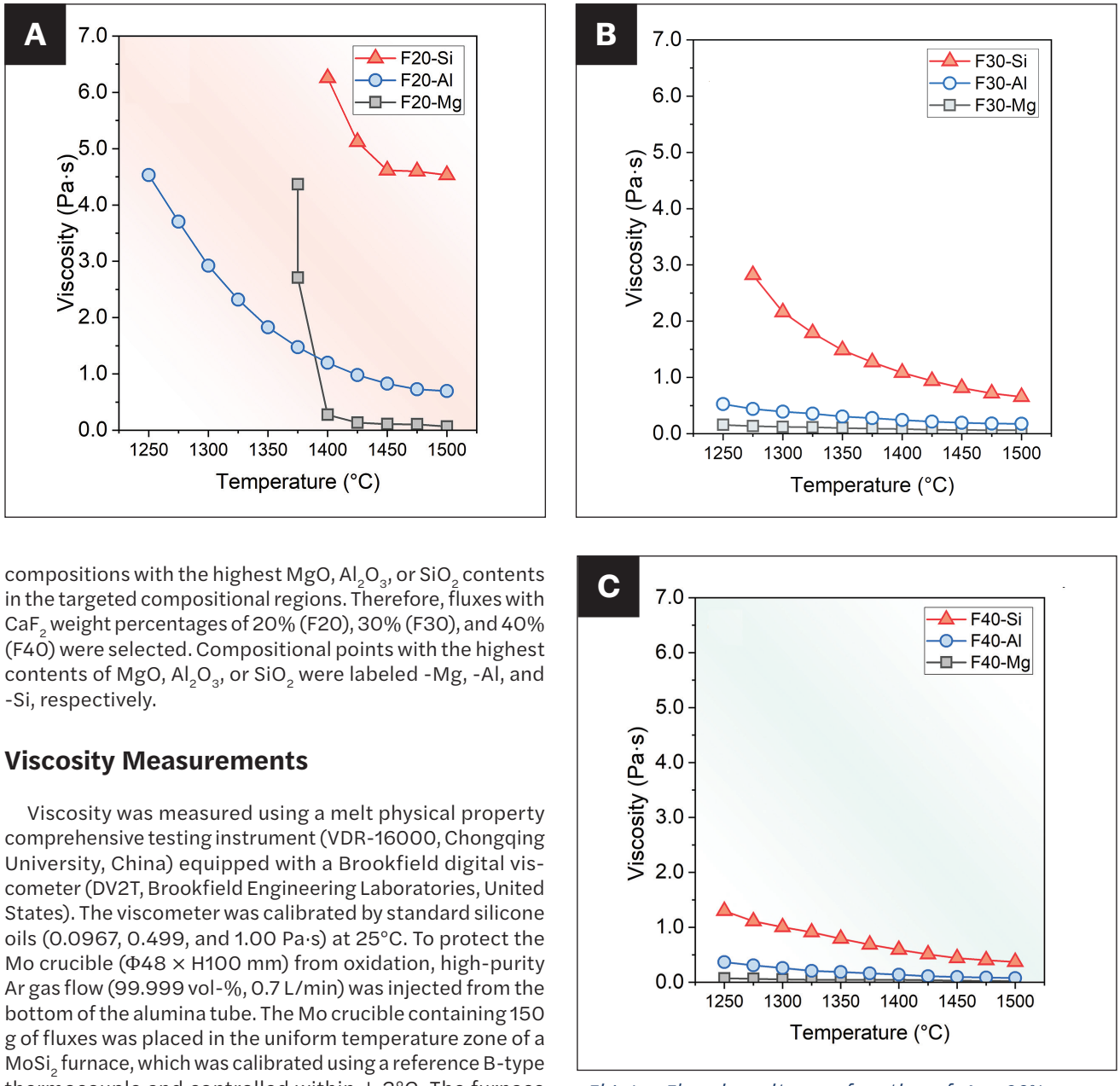

Fig. 1 — Flux viscosity as a function of: A — 20% CaF_2; B — 30% CaF_2; C — 40% CaF_2 at various temperatures.

compositions with the highest MgO, Al_2O_3, or SiO_2 contents in the targeted compositional regions. Therefore, fluxes with CaF_2 weight percentages of 20% (F20), 30% (F30), and 40% (F40) were selected. Compositional points with the highest contents of MgO, Al_2O_3, or SiO_2 were labeled -Mg, -Al, and -Si, respectively.

Viscosity Measurements

Viscosity was measured using a melt physical property comprehensive testing instrument (VDR-16000, Chongqing University, China) equipped with a Brookfield digital viscometer (DV2T, Brookfield Engineering Laboratories, United States). The viscometer was calibrated by standard silicone oils (0.0967, 0.499, and 1.00 Pa·s) at 25°C. To protect the Mo crucible (Φ48 × H100 mm) from oxidation, high-purity Ar gas flow (99.999 vol-%, 0.7 L/min) was injected from the bottom of the alumina tube. The Mo crucible containing 150 g of fluxes was placed in the uniform temperature zone of a $MoSi_2$ furnace, which was calibrated using a reference B-type thermocouple and controlled within ± 2°C. The furnace was heated to 1500°C and maintained for 15 min to ensure homogeneity. Subsequently, the furnace was cooled at 25°C intervals and held at each temperature for 15 min. Viscosity values at target temperatures were the average results obtained at three rotation speeds (10, 20, and 30 r/min).

Molecular Dynamic Simulations

Simulation Method

Molecular dynamics simulations were carried out using the LAMMPS package (Ref. 26). The software PACKMOL (Version 20.3.0) was used to obtain different random initial configurations of the targeted system (Ref. 27). Approximately 4000 atoms were subjected to a simulated melt-quench process within a cubic box, the size of which was dictated by flux density. Interaction between atoms was characterized by the Born-Mayer-Huggins (BMH) interatomic potential. The BMH function is expressed as follows:

$$U_{ij}(r) = \frac{Cq_iq_j}{\varepsilon r_{ij}} + A_{ij}e^{-\frac{r_{ij}}{\rho_{ij}}} - \frac{C_{ij}}{r_{ij}^6} + \frac{D_{ij}}{r_{ij}^8} \quad (1)$$

In Equation 1, U_{ij} is the interatomic-pair potential; C is an energy-conversion constant; q_i and q_j are the selected charges; ε is the dielectric constant; r_{ij} is the interatomic distance between the i atom and j atom; and ρ_{ij} is an ionic-pair

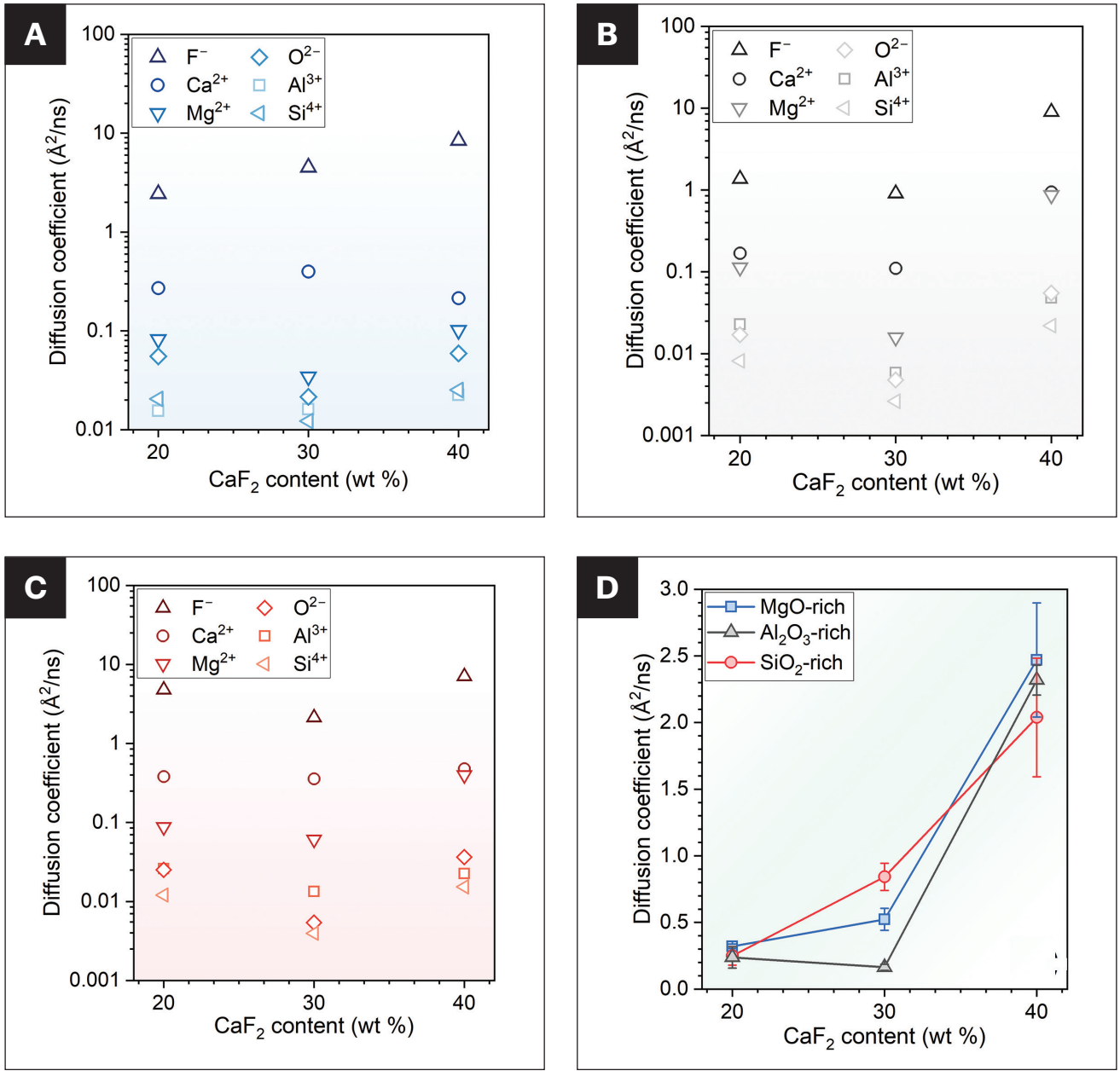

Fig. 2 — Diffusion coefficients of: A — MgO-rich; B — Al_2O_3-rich; C — SiO_2-rich; D — total values at 1500°C.

dependent length parameter. A_{ij}, C_{ij} and D_{ij} are energy parameters of the atom pair. BMH function parameters, which have been proven to be valid through considerable trials, can be found elsewhere (Refs. 21, 28), as can detailed simulation information (Ref. 12). Three parallel simulations were performed for each composition, starting from different initial configurations to ensure statistical reliability.

Diffusion Coefficient Calculation

To calculate transport properties of the flux systems, the mean square displacement curves of each atom were obtained using the following formula:

$$MSD = \langle |r(t) - r(0)|^2 \rangle \quad (2)$$

In this equation, *r(t)* represents the location of an atom at time *t*, and *r(0)* is the starting location of this atom. Then, based on Einstein's Equation, self-diffusion coefficients for varied atoms were calculated as:

$$D_i = \frac{MSD}{6t} \quad (3)$$

$$D_{total} = \sum_{i=0}^{n} D_i \cdot X_i \quad (4)$$

where D_i is the diffusion coefficient of the *i* ion, D_{total} is the total diffusion coefficient, and X_i is the mole fraction of the $_i$ ion.

Bond and Energy Calculation

Distributions of oxygen and fluorine species were calculated using MATLAB software based on the output trajectory profiles from MD simulations. The last frame of the trajectory, consisting of involved atom coordinates, was extracted. Specifically, the first step was to assess whether the bond could be formed. This was determined by comparing the cut-off distance (Rc) with the calculated bond distance. The Rc was determined from radial distribution function curves based on trajectory files. The bond was considered successful if the calculated bond distance was shorter than the Rc. Then, the bonding features of the oxygen atoms could be revealed by performing the loop statements in the MATLAB code. Atom energy data was the sum of potential and kinetic energy extracted from the last 0.5 ns period of the simulations (Ref. 24).

Results

Viscous Behavior Evaluation

Figures 1A–C plot viscosity variations with different CaF_2 contents. Viscosity steadily increased as the temperature decreased; however, as the CaF_2 content increased from 20 to 40%, the peak viscosity at 1500°C (all appearing in SiO_2-rich fluxes) dropped from 4.53 to 0.653 and eventually to 0.371 Pa·s. As the CaF_2 content was constant, the lowest viscosity occurred in the MgO-rich regions, followed by the Al_2O_3-rich regions, with the highest viscosity appearing in SiO_2-rich ones.

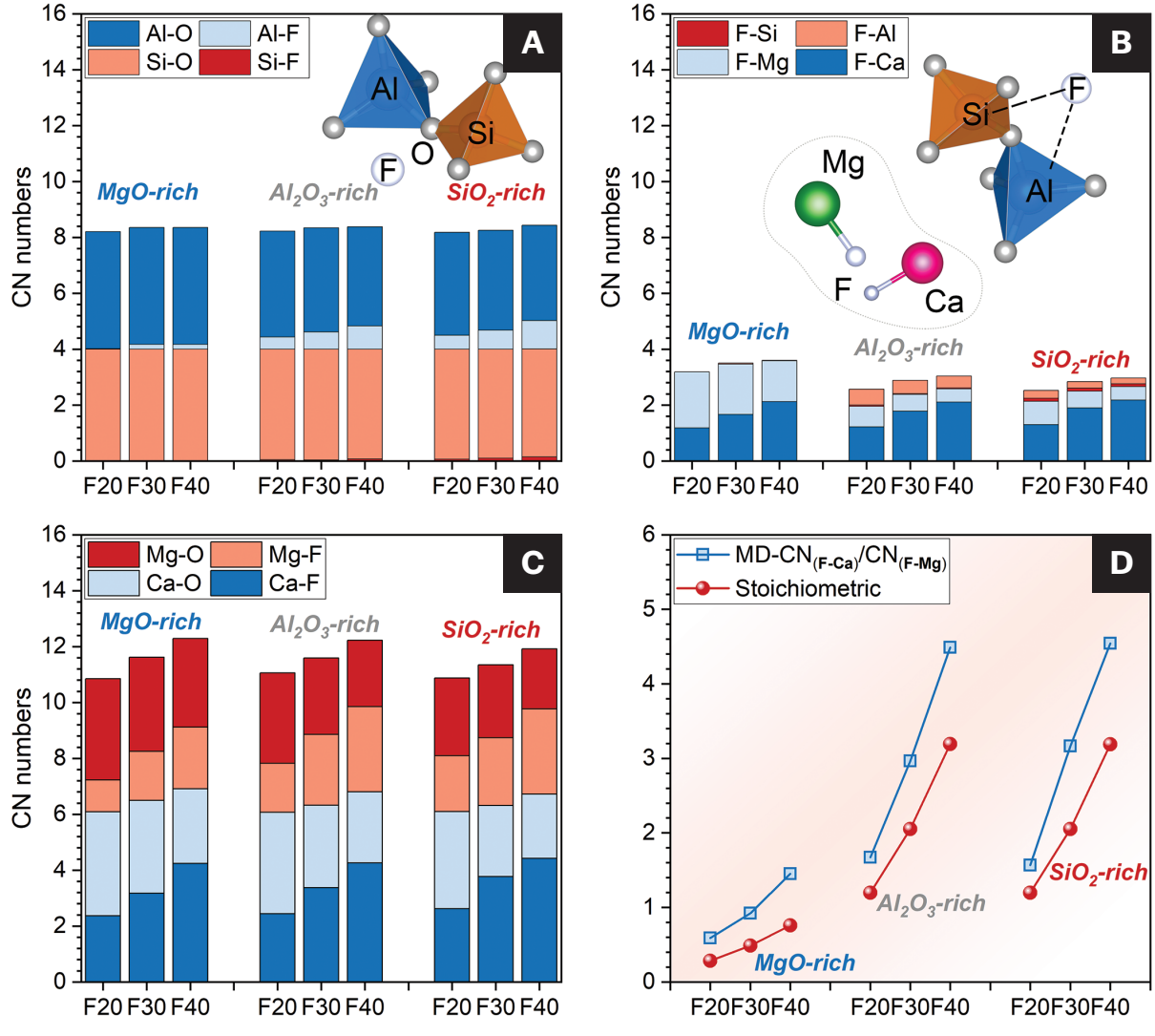

Fig. 3 — A–C — Coordination numbers of involved sites; D — comparison of calculated $CN_{(F\text{-}Ca)}/CN_{(F\text{-}Mg)}$ and theoretical values at 1500°C.

Diffusion Capability Calculation

Liquid phase transport properties can determine viscous behavior from a kinetic perspective. Consequently, ionic diffusion (*D*), a pivotal kinetic parameter, is essential for comprehending microstructure evolution. Figure 2 plots the ionic diffusion coefficients of the ions involved along with total diffusion coefficient values. It was observed that the diffusion coefficient of F^- (D_{F^-}) was significantly higher than the other ions (Figs. 2A–C). Moreover, Ca^{2+} had the second-highest diffusion capability after F^-. In contrast, the diffusion coefficients of Si^{4+}, Al^{3+}, and O^{2-} were similar and considerably lower than that of F^-. Figure 2D shows that patterns of total diffusion coefficient varied with fluoride content. The total diffusion coefficient increased from 0.25 to 2.47 Å^2/ns, with CaF_2 increasing from 20 to 40%. However, at 30% CaF_2 content in the Al-rich region, the F^- and Ca^{2+} diffusion coefficients reached their respective lowest values. In such a composition, the diffusion coefficients of O^{2-} and Si^{4+} were below 0.01 Å^2/ns, significantly lower than those in other regions. However, at a high CaF_2 content (40%), the total diffusion coefficients were considerably higher than those in other fluxes.

Coordination Number Analysis

Coordination number (CN) analysis derived from MD simulations can provide insights into polyhedral and cluster variations. Figure 3 presents CN variations of the involved atoms. In Fig. 3A, the CN of Si-O/F remained consistently at 4.00. The CN of Si-F exhibited only a slight increase (< 0.17) with higher CaF_2 and SiO_2 contents. Moreover, the CNs of the Al atoms ranged between 4.18 and 4.42, which proved that most Al^{3+} exists in tetrahedral coordination, with a minor portion in 5- or 6-coordination. As the CaF_2 content increased from 20 to 40%, the CN of Al-F increased from 0 to a maximum of 1.01, while the CN of Al-O decreased from 4.19 to a

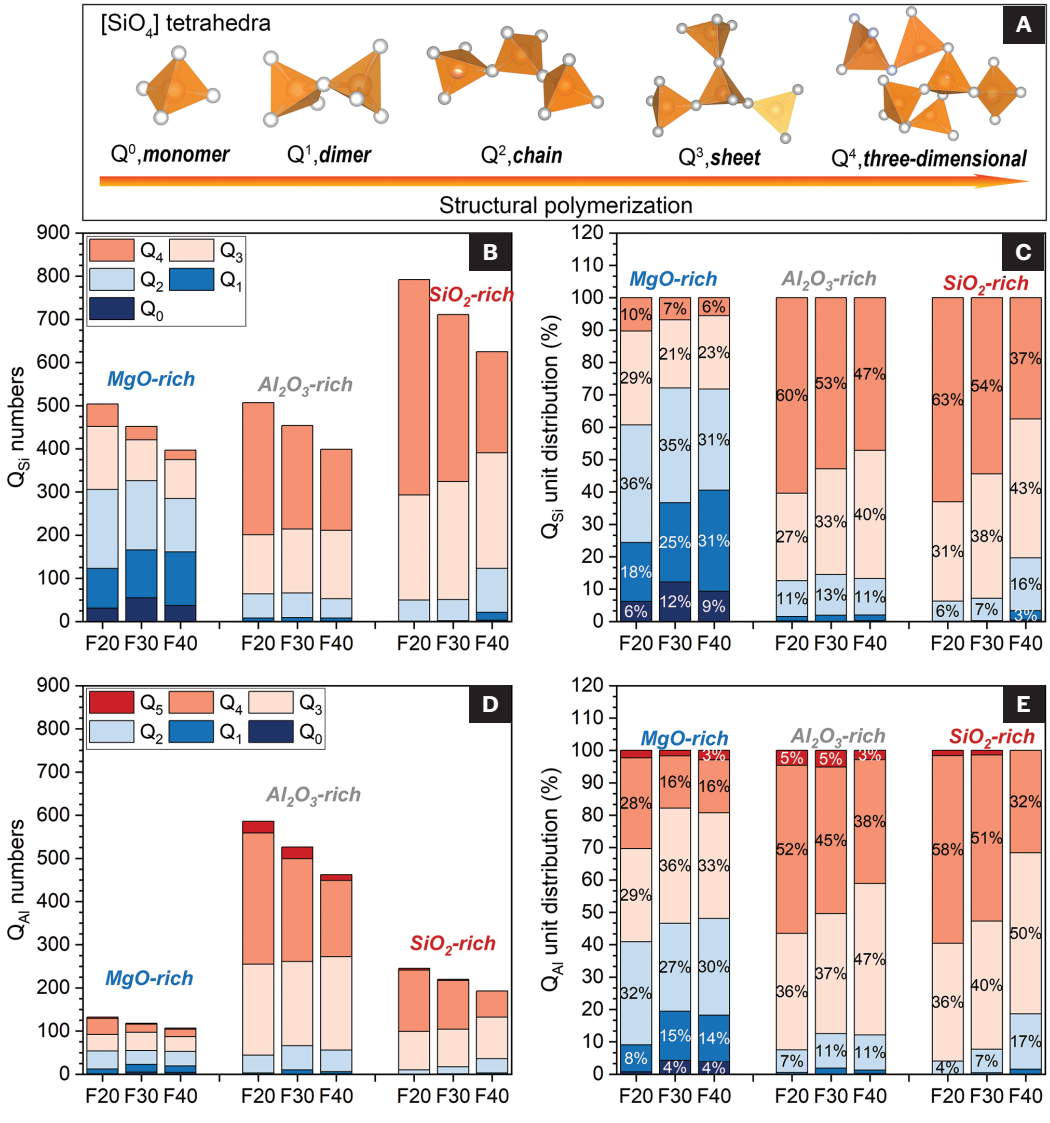

Fig. 4 — A — Schematic diagram of polymerization degree Q^n of [SiO_4] tetrahedra, and number and relative fraction evolutions of B–C — Q^n_{Si}; D–E — Q^n_{Al} at 1500°C.

minimum of 3.41, resulting in an overall increase in the CN of Al. The CN of F-Al was consistently higher than that of F-Si across all compositions (Fig. 3B). The CN of Al-F was less than 0.17 in MgO-rich regions. In the target system, Ca^{2+} and F^- originated exclusively from CaF_2. Theoretically, the atomic ratio of Ca^{2+} to F^- was 1:2. However, as shown in Fig. 3C, the CN of Ca-F ranged from 2.3 to 4.5. With constant CaF_2 content, the CN of Ca-F and F-Ca monotonically increased as the region transitioned from MgO-rich to Al_2O_3-rich to SiO_2-rich regions. In addition, a significant portion of the Mg^{2+} bonded with F^-. To determine if there was preferential bonding of F^- with Mg^{2+} or Ca^{2+}, $CN_{(F\text{-}Ca)}/CN_{(F\text{-}Mg)}$ values obtained by the standard stoichiometric method were compared with MD calculations (Fig. 3D). The calculated values consistently exceeded the stoichiometric ratios.

Polyhedra and Cluster Evolution

Polyhedral Structure Distribution

The discussion above concerned local structures and bonding preferences within polyhedra and clusters. However, polyhedral configurations are imperfect, with Si and Al frequently being undercoordinated, resulting in a sizable number of vacancies. The degree of polymerization of polyhedra is typically measured by the Q_n parameter, where *n* denotes the number of bridging oxygens (BO) around the central atom of the polyhedron (Ref. 29), as shown in Fig. 4A. Prior studies have confirmed that undercoordinated polyhedral structures are less compact but more fluid (Refs. 25, 30). Therefore, it is essential to examine the internal integrity of polyhedra.

Figure 4 illustrates the Q_n unit numbers and distributions for [SiO_4] and [AlO_n] polyhedra. The addition of CaF_2 diluted the overall matrix by proportionally reducing other components. Earlier work has shown that CaF_2 may hardly modify the bonding configuration of [SiO_4] tetrahedra (Ref. 31). However, CaF_2 incrementally reduced the quantity of Q_{si}^n units (Fig. 4B) and altered corresponding relative proportions (Fig. 4C). For example, Q_{si}^0 and Q_{si}^1 units in MgO-rich regions constituted approximately 40% in F30 and F40 but only 3% in F20. Additionally, in SiO_2-rich regions, increasing the CaF_2 content from 20 to 30–40% reduced Q_{si}^4 units from 63 to 37%, aligning with observed viscous changes. Furthermore, Q_{si}^4 unit proportion was relatively high in the Al_2O_3-rich regions due to the Al avoidance principle, where Al-related structures tend to bond with Si-related structures, leading to more complete Si bonding and an increase in Q_{si}^n units.

It has been established that Ca^{2+} cations can disrupt [AlO_n] polyhedra and balance charges. Consequently, analyzing Q_{Al}^n distributions can help identify individual contributions of such effects. Figure 4D shows that CaF_2 diluted units and reduced highly polymerized Q_{Al}^n units (> 4) in all samples. Moreover, the relative proportion of low Q_{Al}^n units increased markedly in all regions (Fig. 4E), indicating that a significant number of Ca^{2+} and Mg^{2+} cations depolymerized the network. Conversely, the high quantity and proportion of high Q_{Al}^n units in the Al_2O_3-rich regions suggest a stronger charge compensation effect.

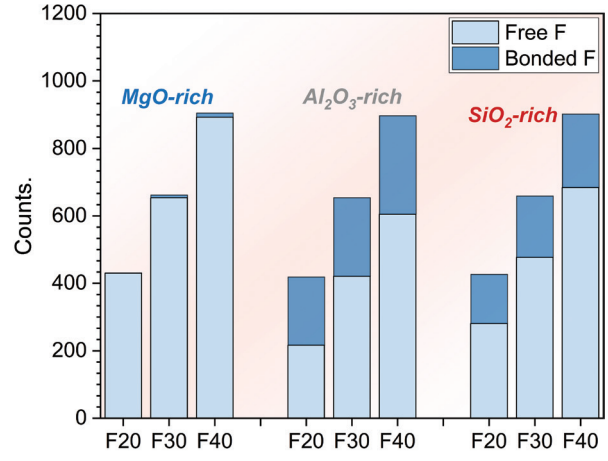

Fig. 5 — Numbers of various bonding types of F atoms at 1500°C.

Cluster Distribution

The influence of F on specific bonding patterns within polyhedral structures has been examined, but it is also essential to elucidate the pertinent impact on clusters. Based on the bonding patterns of oxygen, fluorine can be categorized into two types: bonded fluorine (BF, bonded to a network former) and free fluorine (FF, not bonded to any network former) (Ref. 24). The primary clusters are (Ca, Mg)-FF in the target system. Figure 5 illustrates the quantity changes of different types of F atoms. It can be observed that CaF_2 introduction significantly facilitated FF unit formations, leading to a monotonous increase in fluorine clusters. Among the compositions, the MgO-rich region contained the highest amount of FF units. Combined with earlier O analysis, the structure in the MgO-rich region was highly depolymerized, containing the most FO and FF units. This indicated that F entirely detached from the polyhedral structure, forming numerous fluoride clusters. In contrast, certain BF units remained in Al_2O_3-rich and SiO_2-rich regions, with Al_2O_3-rich regions having more BF units.

Figure 6 depicts structural evolution in distinct regions. In MgO-rich regions with 30% CaF_2, the network was highly depolymerized as separated polyhedra primarily connected via short chains, whereas FF associated with Ca^{2+} and Mg^{2+} to create (Mg, Ca)-F clusters. In Al_2O_3-rich regions, numerous Al-related structural units bonded closely with [SiO_4] polyhedra and, thus, formed a highly polymerized network. In addition, F^- began to bond with Al^{3+}, transforming from FF to BF units. At higher SiO_2 contents, the network was predominantly composed of [SiO_4] polyhedra. As the CaF_2 content increased, a noticeable rise in fluorine clusters appeared. Due to the abundance of SiO_2, [SiO_4] polyhedra chains remained relatively intact. Such structural features corresponded with the statistical results shown in Fig. 3. It was observed that clusters tended to be distributed away from rigid polyhedral structures, leading to more random and uneven cluster distribution in areas with high polyhedral concentrations. Conversely, the cluster distribution was more uniform when short chains connected polyhedra.

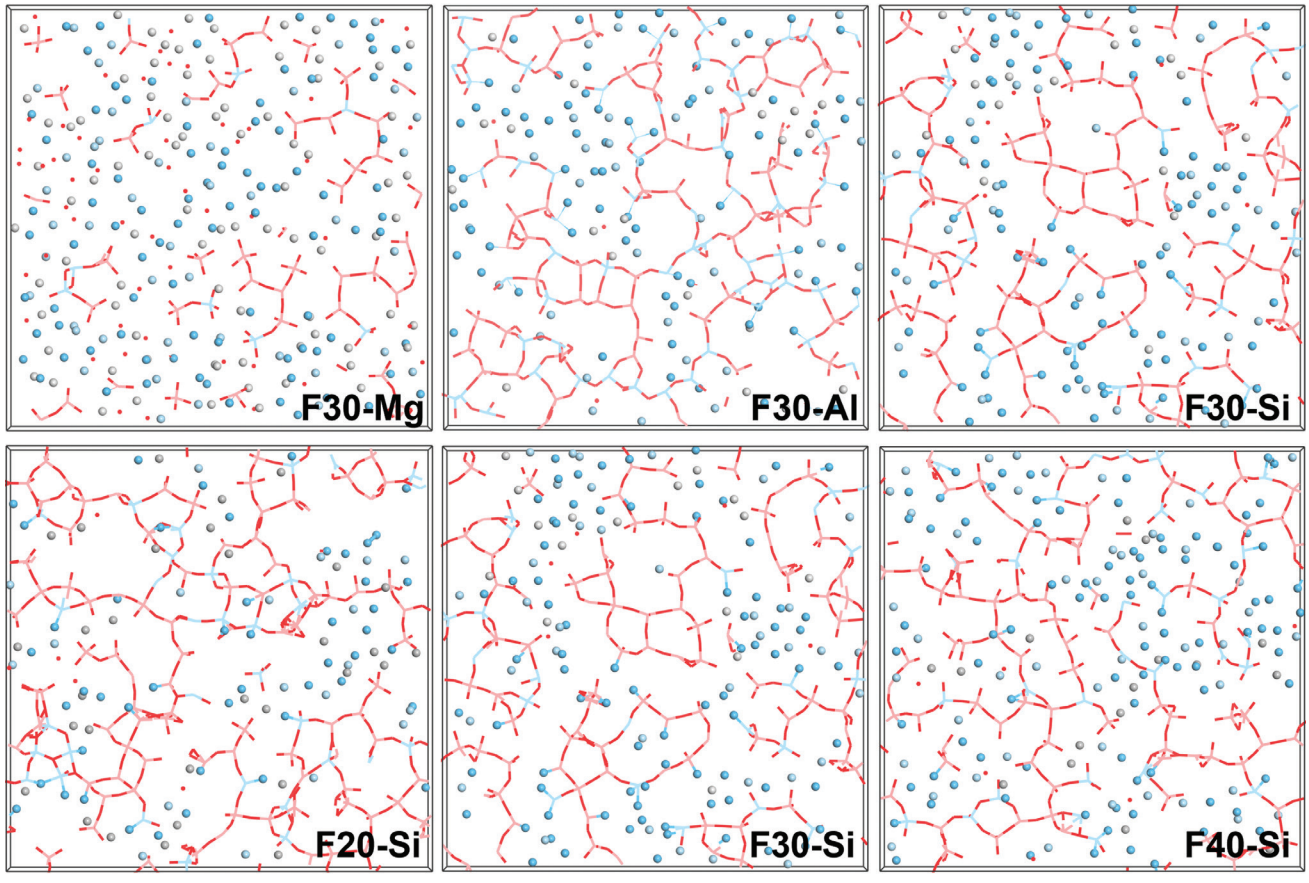

Fig. 6 — Visualization of flux structure evolution from MgO-rich to Al_2O_3-rich to SiO_2-rich, and increased CaF_2 contents from 20 to 30 to 40%. Snapshots were taken from slabs sliced with a thickness of five Å. Red lines represent Si-O bonds, and blue lines represent Al-O bonds, with F atoms shown in blue, Ca atoms in light blue, Mg atoms in light yellow, and O atoms in red.

Discussion

Viscosity Changes Under Different Temperatures and Compositions

The increase in viscosity with decreasing the temperature in Fig. 1 was largely due to reduced thermal vibrations and rigid unit formations. Consensus on optimal viscosity for fluxes has yet to be reached. Still, several studies suggest that a viscosity below 0.6 Pa·s at 1400–1500°C is essential for exceptional flux fluidity and deposition (Refs. 9, 32). Thus, F20-Si viscosity far exceeds recommended limits, which strongly deteriorates weldability. The results demonstrated that CaF_2 can significantly reduce the overall viscosity, although such an effect may diminish at higher CaF_2 levels (40%). SiO_2 and Al_2O_3 contents represent relative proportions of tetrahedra, which are more polymerized than network modifiers, leading to higher viscosity values in SiO_2-rich and Al_2O_3-rich regions. Furthermore, only the viscosity-temperature curve for F20-Mg showed a sharp increase at lower temperatures. Such phenomenon can be attributed to differences in crystallization phases and significant phase precipitation (Ref. 33). Under welding conditions, it is recognized that viscous behavior at high temperatures is more critical. The mechanisms by which CaF_2 influences the viscosity of fluxes with different dominant components will be further elaborated below.

Effect of CaF_2 Addition on Diffusion Capability

It can be conceived that the total diffusion coefficient predominantly depends on the relative proportion of F^-, which is consistent with previous findings (Ref. 7). The Ca^{2+} and F^- diffusion coefficients exhibit a consistent pattern, suggesting coupled diffusion between these ions and supporting the presence of CaF_n clusters (Ref. 7). The lower diffusion coefficients of O^{2-} and Si^{4+} demonstrate that the diffusion capability of clusters can be significantly superior to that of polyhedra. These findings suggest that a denser Al and Si polyhedral structure markedly inhibits ion diffusion, potentially increasing flux viscosity (Ref. 34). Hence, excess CaF_2 clusters create voids between polyhedra, facilitating the migration of all ions. In this system, Ca^{2+} and Mg^{2+} cations act as network modifiers that disrupt Si-O and Al-O bonds, promoting ion migration capability. As illustrated in Fig. 2, the diffusion coefficient of Ca^{2+} was consistently higher than that of Mg^{2+}, which correlated with Ca^{2+} having a higher opti-

Table 2 — Atomic Energy Values in Various Bonds (eV)					
BO	Type	Si-O-Si	Si-O-Al	Al-O-Al	
	Energy	−26.840	−24.854	−22.858	
NBO	Type	Si-O-Ca	Si-O-Mg	Al-O-Ca	Al-O-Mg
	Energy	−23.585	−23.455	−22.008	−21.946
FO	Energy	−22.082			
TO	Type	SiAlAl	AlAlAl		
	Energy	−25.944	−23.649		
FF	Type	Ca-F	Mg-F		
	Energy	−4.464	−4.432		
BF	Type	Si-F	Al-F		
	Energy	−6.050	−4.728		

cal basicity of 1.0. Such higher basicity enhances network disruption, which in turn leads to a reduction in viscosity.

Formation of Polyhedra and Clusters

The CN of Si-O/F remained consistently at 4.00, indicating that Si is predominantly in a tetrahedral configuration. F^- can hardly dope into [SiO_4] tetrahedra since the CN of Si-F exhibited only a slight increase (< 0.17) with higher CaF_2 and SiO_2 contents (Fig. 3A). The CN of Al-O/F demonstrated that certain F^- successfully substituted O^{2-} within [AlO_n] polyhedra. Based on the results of CN values of F-Al/Si, it can be confirmed that F^- preferentially bonds with Al^{3+} and, thus, dopes into [AlO_n] polyhedra (Fig. 3B). The F^- additions reduced the absolute fractions of [SiO_4] and [AlO_n] polyhedra, diluting the aluminosilicate network while simultaneously replacing O^{2-} within [AlO_n] polyhedra.

The CN of Al-F was less than 0.17 in MgO-rich regions, which indicated limited F^- trickling into [AlO_n] polyhedra. In this case, the dilution effect of CaF_2 on O-related structures shall prevail. Conversely, the doping effect of CaF_2 was more pronounced in other regions. It should be noted that the Al-F bond length was approximately 2 Å, higher than that of the Al-O bond (1.75 Å), rendering Al-F bonds less stable. Thus, F doping in [AlO_n] polyhedra can reduce structural symmetry and rigidity. The CN of Ca-F ranged from 2.3 to 4.5, suggesting that certain oxide polyhedra embrace Ca^{2+} sites (Fig. 3C). Such cations acted as network modifiers or charge compensators. In contrast, others resided in F-rich regions, forming CaF_n clusters. Meanwhile, the polyhedral structures became more rigid and randomly generated vacancies, facilitating cluster formation. The significant bonding of Mg^{2+} with F^- demonstrated that network modifiers (Ca^{2+} and Mg^{2+}) prefer

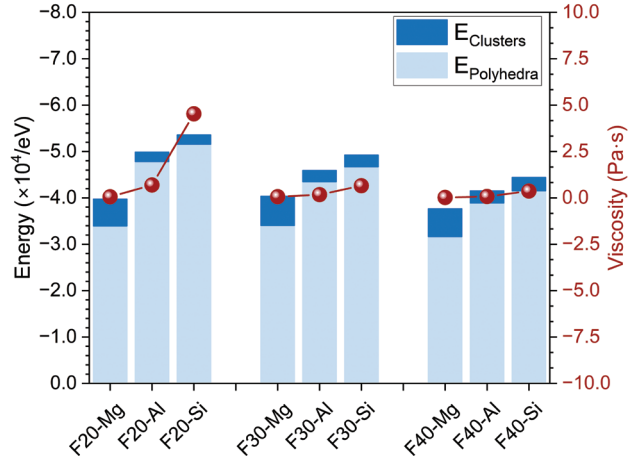

Fig. 7 — Viscosity contribution from polyhedra and clusters.

to bond with F^- rather than with network formers (Si^{4+} and Al^{3+}). Consequently, although rigid polyhedra were more prevalent in SiO_2- and Al_2O_3-rich regions than in MgO-rich ones, corresponding fluoride clusters increased simultaneously. The calculated values of $CN_{(F\text{-}Ca)}/CN_{(F\text{-}Mg)}$ consistently exceeded the stoichiometric ratios, which means F^- tended to bond with Ca^{2+} rather than Mg^{2+}, especially in Al_2O_3- and SiO_2-rich regions with higher CaF_2 contents (Fig. 3D). Therefore, the formation of CaF_n clusters was more favorable than that of MgF_n ones. Furthermore, Fig. 4 suggests that adding CaF_2 not only dilutes the Si-related structure but also significantly restrains the formation of highly polymerized Q_{Si}^n units.

Relationships Between Viscosity and Polyhedra/Clusters

Although polyhedron and cluster information have been quantified, separating respective contributions to viscosity remains challenging. The atomic energy of O and F indicates bond stability, with lower energy correlating with more stable bonds and, consequently, higher viscosity (Ref. 11). By quantifying bond energy, the contributions of polyhedra and clusters to viscosity can be differentiated. Specifically, polyhedral contributions arise from bridging oxygen, non-bridging oxygen (NBO), and bonded fluorine (BF). In contrast, cluster contributions are attributed to the dilution effect by free fluorine and depolymerization of polyhedra through free oxygen (FO). The contributions from polyhedra and clusters can be expressed as follows:

$$E_{polyhedra} = \sum E_O n_O + \sum E_{BF} n_{BF} \quad (5)$$

$$E_{clusters} = \sum E_{FF} n_{FF} + \sum E_{FO} n_{FO} \quad (6)$$

where $E_{polyhedra}$ and $E_{clusters}$ represent the energy of polyhedra and clusters, respectively. E_O, E_{BF}, and E_{FF} are energy of O (BO and NBO), bonded F, and free F units, respectively. n_O, n_{BF}, and n_{FF} are numbers of O (BO and NBO), bonded F, and free F units, respectively. Detailed atom energy values in various bonds are provided in Table 2.

Figure 7 illustrates the energy levels of the polyhedra and clusters along with respective contributions to viscosity at 1500°C. It is evident that energy variations closely mirrored the trends in viscosity. Across different CaF_2 concentrations, the overall system energy followed the order of SiO_2-rich < Al_2O_3-rich < MgO-rich regions, indicating that SiO_2-rich structures were the most energetically stable. Specifically, polyhedra contributed the most to viscosity, while the impact of clusters was relatively minor. However, the contribution from clusters slightly increased with higher CaF_2 content. It is important to note that the smaller contribution of clusters to viscosity does not imply that CaF_2 had a negligible effect. The addition of CaF_2 significantly diluted and altered the internal structure of polyhedra. Such effect was particularly pronounced in SiO_2- and Al_2O_3-rich regions, where polyhedra energy decreased substantially with increasing CaF_2 contents, while the energy change was insignificant in MgO-rich systems. It is suggested that more-complex and polymerized polyhedra are more susceptible to the influence of CaF_2, leading to more-pronounced viscosity fluctuations.

Implications

Microstructural evolution determines trends in flux viscosity at high temperatures. Therefore, the present investigation aimed to establish a relationship between composition, structure, and viscosity, enabling precise and targeted control of flux viscosity. This work was the first step toward correlating different flux viscosity with actual welding performance. We will then evaluate weld shapes and alloying element transfer behaviors at various viscosity levels, connecting the present findings to practical flux design. It is important to note that differentiating the contributions of individual flux properties to welding performance poses a significant challenge, which will be a key focus for our future endeavors.

Conclusions

The structural role of CaF_2 on the viscosity of CaF_2–SiO_2–Al_2O_3–MgO fluxes was investigated based on experiments and theoretical calculations. Our conclusions are as follows.

1. As the CaF_2 content increases from 20 to 40%, the maximum viscosity at 1500°C decreases from 4.53 to 0.375 Pa·s. Such reduction could be partly attributed to the dilution of structure and inhibition of highly polymerized units, which significantly improves atomic diffusion capabilities. At a fixed CaF_2 content, viscosity values follow the order of SiO_2-rich > Al_2O_3-rich > MgO-rich regions.

2. CaF_2 alters Q_n unit distributions of Si and Al polyhedra in addition to the diluting polyhedral network. Certain F^- replace O^{2-} bonded to Al^{3+}, while certain Ca^{2+} ions act as network modifiers, disrupting highly polymerized Q_n units. The introduced F^- tends to incorporate into [AlO_n] polyhedra, with Ca^{2+} providing stronger structural compensation in Al_2O_3-rich environments.

3. Compared with clusters, polyhedra contribute more significantly to viscosity variations. Complex and polymerized polyhedra are susceptible to CaF_2 additions, leading to more pronounced viscosity fluctuations.

Acknowledgments

The authors sincerely acknowledge the financial support from the National Key R&D Program of China (Grant Nos. 2023YFB3709900 and 2022YFE0123300), the National Natural Science Foundation of China (Grant Nos. W2411047, 52404393, and U20A20277), and the Fundamental Research Funds for the Central Universities (Grant No. N2402016).

References

1. Wang, C., and Zhang, J. 2021. Fine-tuning weld metal compositions via flux optimization in submerged arc welding: An overview. *Acta Metallurgica Sinica* 57(9): 1126–1140. DOI: 10.11900/0412.1961.2021.00148

2. Sengupta, V., Havrylov, D., and Mendez, P. F. 2019. Physical phenomena in the weld zone of submerged arc welding–A review. *Welding Journal* 98: 283-s to 313-s. DOI: 10.29391/2019.98.025

3. Han, C., Zhong, M., Zuo, P., and Wang, C. 2024. SiO_2-bearing fluxes induced evolution of γ columnar grain size. *Welding Journal* 103(12): 362-s to 371-s. DOI: 10.29391/2024.103.031

4. Kurlanov, S. A., Potapov, N. N., and Natapov, O. B. 1993. Relationship of physical and welding-technological properties of fluxes for welding low-alloy steels. *Welding International* 7(1): 65–68. DOI: 10.1080/09507119309548346

5. Schwemmer, D. D., Olson, D. L., and Williamson, D. L. 1979. The relationship of weld penetration to the welding flux. *Welding Journal* 58(5): 153-s to 160-s.

6. Zhang, J., Wang, C., and Coetsee, T. 2021. Assessment of weld metal compositional prediction models geared towards submerged arc welding: Case studies involving CaF_2-SiO_2-MnO and CaO-SiO_2-

MnO fluxes. *Metallurgical and Materials Transactions B* 52(4): 2404–2415. DOI: 10.1007/s11663-021-02190-x

7. Yuan, H., Wang, Z., Zhang, Y., Basu, S., Li, Z., and Wang, C. 2024. Uncovering crystallization mechanisms of SiO_2–MnO based welding fluxes. *Journal of Non-Crystalline Solids* 627: 122824. DOI: 10.1016/j.jnoncrysol.2024.122824

8. Zhang, Y., Wang, Z., Zhang, J., Li, Z., Basu, S., and Wang, C. 2022. Probing viscosity and structural variations in CaF_2–SiO_2–MnO welding fluxes. *Metallurgical and Materials Transactions B* 53(5): 2814–2823. DOI: 10.1007/s11663-022-02566-7

9. Wang, Z., Li, Z., Zhong, M., Li, Z., and Wang, C. 2023. Elucidating the effect of Al_2O_3/SiO_2 mass ratio upon SiO_2-MnO-CaF_2-Al_2O_3-based welding fluxes: Structural analysis and thermodynamic evaluation. *Journal of Non-Crystalline Solids* 601: 122071. DOI: 10.1016/j.jnoncrysol.2022.122071

10. He, C., Fan, F., Guo, J., Yuan, M., Qin, Y., Wei, Y., and Yan, J. 2024. Viscosity determination of the biomass slag in the SiO_2-CaO-K_2O system based on the bond distribution. *Fuel* 356: 129642. DOI: 10.1016/j.fuel.2023.129642

11. Xuan, W., Guhl, S., Zhang, Y., Zhang, J., and Meyer, B. 2022. A structural viscosity model for silicate slag melts based on MD simulation. *Ceramics International* 48(19): 28291–28298. DOI: 10.1016/j.ceramint.2022.06.136

12. Yuan, H., Wang, Z., Zhang, Y., and Wang, C. 2023. Roles of MnO and MgO on structural and thermophysical properties of SiO_2-MnO-MgO-B_2O_3 welding fluxes: A molecular dynamics study. *Journal of Molecular Liquids* 386: 122501. DOI: 10.1016/j.molliq.2023.122501

13. Zhang, Y., Yuan, H., Tian, H., Wang, Z., and Wang, C. 2023. Elucidating electrical conductive mechanisms for CaF_2–SiO_2–CaO–TiO_2 welding fluxes. *Metallurgical and Materials Transactions B* 54(6): 3023–3030. DOI: 10.1007/s11663-023-02885-3

14. Zhang, C., Wu, T., Ren, P., Shi, H., Liao, Z., and Wang, H. 2023. Influence mechanism of F^- on the structure and properties of aluminate-based mold flux. *Metallurgical and Materials Transactions B* 54(5): 2784–2792. DOI: 10.1007/s11663-023-02874-6

15. Zhang, G. H., and Chou, K. C. 2013. Influence of CaF_2 on viscosity of aluminosilicate melts. *Ironmaking & Steelmaking* 40(5): 376–380. DOI: 10.1179/1743281212y.0000000055

16. Tian, H., Wang, Z., Zhao, T., and Wang, C. 2022. A Raman and multinuclear ^{29}Si, ^{27}Al, and ^{19}F NMR study on the structural roles of CaF_2 in SiO_2–CaO–Al_2O_3-based welding fluxes. *Metallurgical and Materials Transactions B* 53: 232–241. DOI: 10.1007/s11663-021-02359-4

17. Zeng, Q., and Stebbins, J. F. 2000. Fluoride sites in aluminosilicate glasses: high-resolution 19F NMR results. *American Mineralogist* 85(5–6): 863–867.

18. Brauer, D. S., Karpukhina, N., Law, R. V., and Hill, R. G. 2009. Structure of fluoride-containing bioactive glasses. *Journal of Materials Chemistry* 19(31): 5629–5636

19. Sahu, P., Pente, A. A., Singh, M. D., Chowdhri, I. A., Sharma, K., Goswami, M., Ali, S. M., Shenoy, K. T., and Mohan, S. 2019. Molecular dynamics simulation of amorphous SiO_2, B_2O_3, Na_2O-SiO_2, Na_2O-B_2O_3, and Na_2O-B_2O_3-SiO_2 glasses with variable compositions and with Cs_2O and SrO dopants. *Journal of Physical Chemistry B* 123(29): 6290–6302. DOI: 10.1021/acs.jpcb.9b03026

20. Bi, Z., Li, K., Jiang, C., Zhang, J., and Ma, S. 2021. Effects of amphoteric oxide (Al_2O_3 and B_2O_3) on the structure and properties of SiO_2-CaO melts by molecular dynamics simulation. *Journal of Non-Crystalline Solids* 559: 120687. DOI: 10.1016/j.jnoncrysol.2021.120687

21. Wang, Z., Huang, S., Yu, Y., Wen, G., Tang, P., and Hou, Z. 2021. Comprehensive understanding of the microstructure and volatilization mechanism of fluorine in silicate melt. *Chemical Engineering Science* 243: 116773. DOI: 10.1016/j.ces.2021.116773

22. Christie, J. K. 2023. Clustering of fluoride and phosphate ions in bioactive glass from computer simulation. *Philosophical Transactions of the Royal Society A: Mathematical, Physical and Engineering Sciences* 381(2258): 20220345. DOI: 10.1098/rsta.2022.0345

23. Christie, J. K., Pedone, A., Menziani, M. C., and Tilocca, A. 2011. Fluorine environment in bioactive glasses: ab Initio molecular dynamics simulations. *Journal of Physical Chemistry B* 115(9): 2038–2045. DOI: 10.1021/jp110788h

24. Yuan, H., Zhang, Y., Liu, H., Li, Z., and Wang, C. 2025. Bond characteristic-dependent viscosity variations in CaF_2-SiO_2-Al_2O_3-MgO welding fluxes. *Welding Journal* 104(4): 107-s to 118-s. DOI: 10.29391/2025.104.009

25. Mills, K. C., Yuan, L., and Jones, R. T. 2011. Estimating the physical properties of slags. *Journal of the Southern African Institute of Mining and Metallurgy* 111: 649–658.

26. Plimpton, S. 1995. Fast parallel algorithms for short-range molecular dynamics. *Journal of Computational Physics* 117(1): 1–19.

27. Martinez, L., Andrade, R., Birgin, E. G., and Martinez, J. M. 2009. PACKMOL: A package for building initial configurations for molecular dynamics simulations. *Journal of Computational Chemistry* 30(13): 2157–2164. DOI: 10.1002/jcc.21224

28. Fan, H., Wang, R., Duan, H., Chen, D., and Xu, Z. 2021. Structural and transport properties of TiO_2-SiO_2-MgO-CaO system through molecular dynamics simulations. *Journal of Molecular Liquids* 325: 115226. DOI: 10.1016/j.molliq.2020.115226

29. Giordano, D., and Russell, J. K. 2018. Towards a structural model for the viscosity of geological melts. *Earth and Planetary Science Letters* 501: 202–212. DOI: 10.1016/j.epsl.2018.08.031

30. Jahn, S. 2022. Molecular simulations of oxide and silicate melts and glasses. *Reviews in Mineralogy and Geochemistry* 87(1): 193–227. DOI: 10.2138/rmg.2022.87.05

31. Zhang, X., Liu, C., and Jiang, M. 2020. Effect of fluorine on melt structure for CaO–SiO_2–CaF_2 and CaO–Al_2O_3–CaF_2 by molecular dynamics simulations. *ISIJ International* 60(10): 2176–2182. DOI: 10.2355/isijinternational.ISIJINT-2020-002

32. Wang, Z., Zhang, J., Zhong, M., and Wang, C. 2022. Insight into the viscosity-structure relationship of MnO–SiO_2–MgO–Al_2O_3 fused submerged arc welding flux. *Metallurgical and Materials Transactions B* 53: 1364–1370. DOI: 10.1007/s11663-022-02507-4

33. Kong, L., Bai, J., and Li, W. 2021. Viscosity-temperature property of coal ash slag at the condition of entrained flow gasification: A review. *Fuel Processing Technology* 215: 106751. DOI: 10.1016/j.fuproc.2021.106751

34. Zhang, L., Song, X., Wei, J., Yang, J., Lv, P., Su, W., Zhou, Y., and Yu, G. 2023. Simulation and experimental study on the effect of iron on the structure and flow properties of coal ash slag. *Chemical Engineering Science* 273: 118642. DOI: 10.1016/j.ces.2023.118642

HANG YUAN, **YANYUN ZHANG**, and **CONG WANG** (*wangc@smm.neu.educn*) are with Key Laboratory for Ecological Metallurgy of Multimetallic Mineral (Ministry of Education), Northeastern University, Shenyang, China, and the School of Metallurgy, Northeastern University, Shenyang, China. **YANQING ZHAO** and **JIE LI** are with HBIS Materials Technology Research Institute, Shijiazhuang, China. **ZUSHU LI** is with WMG, University of Warwick, Coventry, United Kingdom.